Modelling of a Cantilevered Energy Harvester with Partial Piezoelectric Coverage and Shunted to Practical Interface Circuits

Guobiao HU[1], Lihua TANG*[1], Junrui LIANG[2], Raj DAS[3]

[1] Department of Mechanical Engineering, University of Auckland, 20 Symonds Street, Auckland 1010, New Zealand
[2] School of Information Science and Technology, ShanghaiTech University, 393 Middle Huaxia Road, Shanghai 201210, China
[3] School of Engineering, RMIT University, GPO Box 2476, Melbourne, VIC 3001, Australia
* Corresponding author, l.tang@auckland.ac.nz

Abstract

This paper presents a modelling methodology for a cantilevered energy harvester with partial piezoelectric coverage and shunted to practical power conditioning interface circuits. Firstly, the distributed parameter model of the partially covered piezoelectric energy harvester is developed and the associated analytical solution is derived. Subsequently, the single-degree-of-freedom (SDOF) representation model is developed and the explicit expressions of equivalent lumped parameters are derived by taking the static-deflection as the approximated fundamental vibration mode. Based on the comparison with the single mode expression of the distributed parameter model, a correction factor is proposed to improve the accuracy of the SDOF model. The results of both the distributed parameter and the corrected SDOF models are compared. The accuracy of the corrected SDOF representation model is verified against the analytical and the finite element models. Finally, practical interface circuits including the standard energy harvesting (SEH) circuit and the parallel synchronized switch harvesting on inductor (P-SSHI) circuit are considered. A modified equivalent impedance modelling (EIM) method is proposed for the analysis of the SEH and P-SSHI circuits. The results of the modified EIM method are verified against the existing method in the literature.

1. Introduction

Vibration energy harvesting has attracted significant research interests in the last decade (Hu et al., 2017; Hu et al., 2018; Tao et al., 2018; Wu et al., 2018; Zhou et al., 2018), as this technology has a promising potential for enabling widely utilized micro-electromechanical systems (MEMS) to substitute for electrochemical batteries in the circumstances where environmental vibrations exist. A comprehensive study of a practical energy harvester often requires the consideration of both mechanical and electrical aspects. Hence, reliable modelling methods for both the mechanical structures and electronic interface circuits constitute the fundamentals aspects of research in this field. In addition, bridging the mechanical and electrical models is essential to achieve accurate estimation.

One of the most typical designs of piezoelectric energy harvesters (PEHs) is a cantilevered beam covered with a single or multiple piezoelectric transducers. When such a structure is excited around its resonance frequencies (especially the fundamental one), the cantilevered PEH could deliver a maximum power output. Several modelling methods have been proposed for describing the behavior of this type of PEHs and predicting the energy harvesting performance. Yang et al. (2009) proposed an equivalent circuit representation for the cantilevered PEH. The advantage of this modelling method is that the equivalent circuit representation of the mechanical structure enables the mechanical and the electrical parts of the PEH system to be bridged, which can incorporate complicated nonlinear circuits. However, in their model, the piezoelectric layer was assumed to cover the entire cantilevered beam. Erturk et al. (2008a) developed the distributed parameter model of the cantilevered PEH and derived the closed-form analytical solution. However, the piezoelectric layer was also assumed to cover the entire substrate. Originated from the distributed parameter solution given by (Erturk et al., 2008a), some researchers adopted the single mode approximation for simplicity (Stanton et al., 2010). The accuracy of the single-mode model in the vicinity of the fundamental mode of interest has been proved (Erturk et al., 2009). As a simpler alternative to the single-mode model, the SDOF model (duToit et al., 2005; Liu et al., 2012; Liu et al., 2016; Priya, 2007; Shu et al., 2006; Tang et al., 2012; Xu et al., 2015; Yang et al., 2013) has been widely adopted by researchers. Although the explicit expressions of the equivalent lumped parameters were provided in (Kim et al., 2011; Shu et al., 2006), the results are valid under the assumption of full piezoelectric coverage. Tang et al. (2012) presented a physical prototype with partial piezoelectric coverage, however, the equivalent lumped parameters were determined from the experiments. Other literature that involves the utilization of the SDOF model includes (Lan et al., 2018a; Lan et al., 2018b; Yang et al., 2013; Zhou et al., 2013), to name a few. Based on the literature review, it is found that though the distributed parameter models of cantilevered energy harvesters with partial piezoelectric coverage have been derived by e.g., (Abdelkefi et al., 2014; Zhao et al., 2015), all the studies of SDOF models have been conducted under the assumption of full piezoelectric coverage. The explicit expressions for the equivalent lumped parameters of the SDOF model of the cantilevered PEH with partial piezoelectric coverage have not been yet derived. Besides the issue of ignoring of partial piezoelectric coverage, Erturk et al. (2007) pointed out that the commonly used SDOF model may yield a significant prediction error and underestimate the dynamic motion of the system. Based on the comparison between the expressions of the transmittances obtained from the analytical and SDOF models, a correction factor has been proposed to improve the accuracy of the SDOF model. However, this work concentrated on only a pure mechanical model without the inclusion of the piezoelectric element (Erturk et al., 2007, 2008b). Thus, the corrected SDOF model is only applicable for predicting the dynamic motion of the cantilevered beam without taking the piezoelectric effect into account. Therefore, the main aim of the present paper is to develop a robust SDOF model of the cantilevered PEH with partially covered piezoelectric layer for predicting energy harvesting performance.

In addition, practical design of a PEH often requires a standard energy harvesting circuit (i.e., an AC-DC interface circuit) (Lefeuvre et al., 2005) to power real applications, or sometimes a complicated nonlinear interface circuit for efficiency improvement, such as synchronized charge extraction (SCE) (Liu et al., 2018; Zhao et al., 2016), synchronized switch harvesting on inductor (SSHI) (Guyomar et al., 2005a; Liang et al., 2012; Shu et al., 2007), etc. The existence of the complicated interface circuits poses difficulties to investigate the energy harvesting performance analytically (Yang et al., 2009). The simplest way to evaluate the power output of a PEH shunted to a SEH interface circuit is to uncouple the mechanical and electrical parts (Shu et al., 2006). However, this method is only valid for weakly coupled systems. A method for estimating the energy harvesting output of a PEH shunted to a SEH or P-SSHI circuit is presented in (Guyomar et al., 2005b) by assuming that the external forcing function and the velocity of the mass are in phase. It can be anticipated that the in-phase assumption is only valid in limited circumstances where the electro-mechanical coupling is not strong and the operating point is around resonance. Shu et al. (2006) later proposed a method to model PEHs with SEH interface circuit that was accurate for both weak and strong couplings. By comparing the simulation and experimental results, the reliability of that method was confirmed. Based on the same approach, Shu et al. (2007) extended this method for the analysis of the Parallel-SSHI interface circuit. From another point of view, by using the harmonic decomposition method and only taking the fundamental component, an equivalent impedance modelling (EIM) method was proposed in (Liang et al., 2012). This method was capable of analyzing the SEH, Parallel-SSHI and Series-SSHI interface circuits even for strong coupling cases. The EIM method represents the interface circuit by an equivalent impedance. The energies consumed by different components of the equivalent impedance have different corresponding physical meanings. Thus the EIM method provides a much clearer view of the energy flow in the energy harvesting system which is the advantage over the method in (Shu et al., 2006; Shu et al., 2007). However, the main drawback of the EIM method is that the final expression of the harvested power is a function of the rectifier block angle and it cannot calculate the rectified voltage. So this paper also aims to improve the EIM method. The improved the EIM method is expected to inherit the advantages of both the original EIM method and the method presented in (Shu et al., 2006; Shu et al., 2007). Together with the proposed SDOF representation method, this paper develops a comprehensive modelling technique of a cantilevered PEH with partial piezoelectric coverage shunted to a SEH/P-SSHI interface circuit.

The rest of this paper is organized as follows: in section 2, the distributed parameter model of the cantilevered energy harvester with partial piezoelectric coverage is developed and the closed-form solution is obtained. The procedure for developing the SDOF model is then demonstrated in section 3. For the sake of simplicity to derive the explicit expressions of several equivalent parameters, the static deflection is used as the approximation of the fundamental vibration mode in the derivation. To further improve the accuracy of the SDOF model, a correction factor is derived to increase the accuracy of prediction of the SDOF model. In section 4, the corrected SDOF model is compared with the distributed parameter model and the finite element model for verification. To include the features of practical interface circuits, a modified EIM method is proposed in section 5 for the analysis of the SEH and P-SSHI interface circuits. The predicted results of the modified EIM method are discussed and compared with those of the methods from (Shu et al., 2006; Shu et al., 2007) in section 6.

2. Distributed parameter model

The distributed parameter model of the partially covered piezoelectric energy harvester and its analytical solution in section 2 are not brand new. Similar work has already been reported in the existing literature such as (Abdelkefi et al., 2014; Zhao et al., 2015). However, for the sake of completeness and the ease of understanding for the readers, the modelling process is reviewed. The subsequent work of developing the simplified SDOF representation model will need to utilize part of the main conclusions derived from the distributed parameter model.

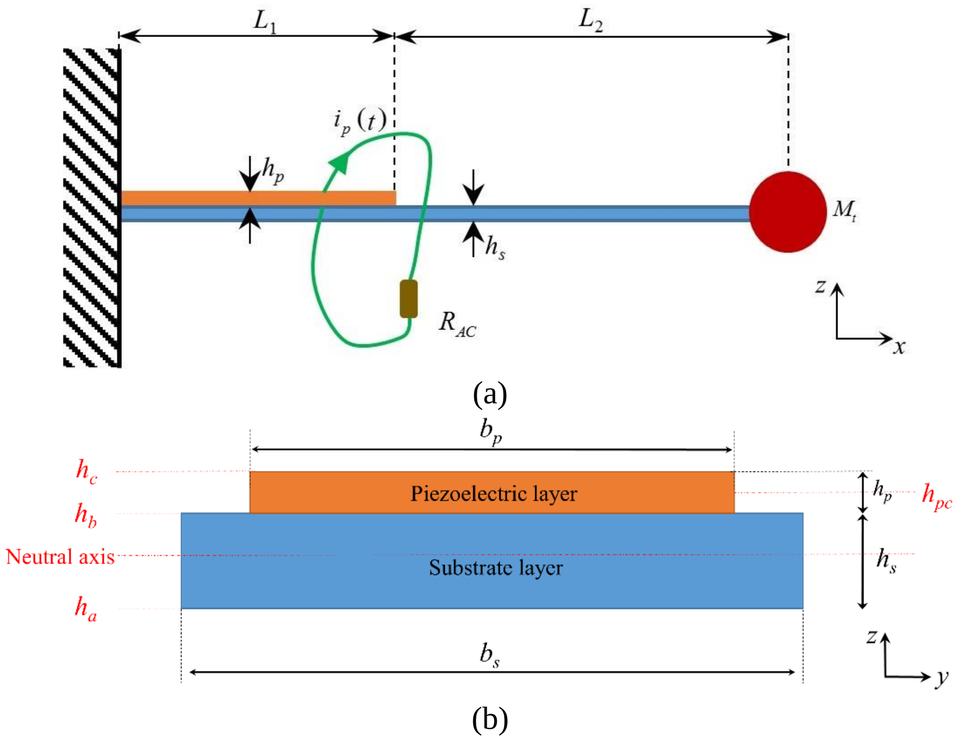

Figure 1. (a) Schematic of the cantilevered PEH with partial piezoelectric coverage; (b) the cross-section view.

The schematic of the system under investigation is shown in Figure 1(a). The left side of the beam is clamped to the base. The thickness and length of the host beam are h_s and L ($L=L_1+L_2$), respectively. It is covered by a piezoelectric layer of thickness h_p and length L_1. The piezoelectric transducer is connected to a resistive load R_{AC}. The subscripts s and p denote the host beam and the piezoelectric layer, respectively. The subscripts 1 and 2 represent the subsections with and without the piezoelectric layer, respectively. A concentrated mass of M_t is attached at the tip of the beam to tune its fundamental natural frequency. Figure 1(b) shows the cross-section view of the beam, where h_a is the position of the bottom of the substrate layer to the neutral axis. The widths of the host beam and the piezoelectric layer are b_s and b_p, respectively. h_b and h_c are the positions of the bottom and top of the piezoelectric layer to the neutral axis, respectively. These position parameters can be calculated from the material and geometric properties of the beam by the following relations.

$$\begin{cases} h_a = -\dfrac{E_p b_p h_p \left(2h_s + h_p\right) + E_s b_s h_s^2}{2\left(E_p b_p h_p + E_s b_s h_s\right)} \\ h_b = h_s + h_a \\ h_c = h_p + h_b \end{cases} \tag{1}$$

where E_s and E_p are the Young's moduli of the host beam and piezoelectric layer, respectively. The cantilevered beam is excited transversely (vertically in z direction) due to the motion of the base ($w_b(t)$). The governing equations of the beam for the sections with and without the piezoelectric layer are written as (Zhao et al., 2013):

$$\begin{cases} EI_1 \dfrac{\partial^4 w_1(x_1,t)}{\partial x_1^4} + m_1 \dfrac{\partial^2 w_1(x_1,t)}{\partial t^2} + \vartheta v(t) \times \left[\dfrac{d\delta(x_1)}{dx_1} - \dfrac{d\delta(x_1 - L_1)}{dx_1} \right] = -m_1 \dfrac{\partial^2 w_b(t)}{\partial t^2} \\ EI_2 \dfrac{\partial^4 w_2(x_2,t)}{\partial x_2^4} + m_2 \dfrac{\partial^2 w_2(x_2,t)}{\partial t^2} = -\left[m_2 + M_t \delta(x_2 - L_2) \right] \dfrac{\partial^2 w_b(t)}{\partial t^2} \end{cases} \tag{2}$$

where $w_1(x_1,t)$ and $w_2(x_2,t)$ represent the relative displacements to the base motion of the beam sections in $0 \le x_1 \le L_1$ and $0 \le x_2 \le L_2$, respectively. $\delta(x)$ is the Dirac delta function, m_1 and m_2 are the mass per unit length and EI_1 and EI_2 are the bending stiffnesses of the two beam sections, ϑ is the piezoelectric coupling term, and $v(t)$ is voltage across the piezoelectric layer. These parameters are determined by the geometric and material properties of the beam as follows.

$$\begin{cases} m_1 = \rho_s h_s b_s + \rho_p h_p b_p \\ m_2 = \rho_s h_s b_s \\ EI_1 = \dfrac{E_s b_s}{3}\left(h_b^3 - h_a^3\right) + \dfrac{E_p b_p}{3}\left(h_c^3 - h_b^3\right) \\ EI_2 = \dfrac{E_s b_s h_s^3}{12} \\ \vartheta = -e_{31} b_p h_{pc} \end{cases} \tag{3}$$

where h_{pc} is the position of the centre of the piezoelectric layer to the neutral axis. e_{31} is the piezoelectric stress constant. The linear-electroelastic constitutive relation for the piezoelectric material is expressed as:

$$D_e(x_1,t) = e_{31} S(x_1,t) + \varepsilon_{33}^S E_3(t) \tag{4}$$

where $S(x_1,t)$ is the bending strain, $D_e(x_1,t)$ is the electric displacement, ε_{33}^S is the permittivity at constant stress. The electric field in the piezoelectric transducer in terms of the voltage across it can be expressed as $E_3(t) = -v(t)/h_p$. According to the Euler-Bernoulli beam theory, the average bending strain in the piezoelectric transducer can be expressed as $S(x_1,t) = -h_{pc}\left[\partial^2 w_1(x_1,t)/\partial x_1^2\right]$. Therefore, Eq.(4) becomes:

$$D_e\left(x_1,t\right)=e_{31}h_{pc}\frac{\partial^2 w_1\left(x_1,t\right)}{\partial x_1^2}-\varepsilon_{33}^S\frac{v(t)}{h_p} \tag{5}$$

Integrating the electric displacement over the electrode area and then differentiating with respect to time provides the current $i_p(t)$ flowing out of the piezoelectric transducer as follows:

$$i_p(t)=\vartheta\int_{x_1=0}^{L_1}\frac{\partial^3 w_1\left(x_1,t\right)}{\partial x_1^2\partial t}dx-C_p\frac{dv(t)}{dt} \tag{6}$$

where $C_p=\varepsilon_{33}^S bL_1/h_p$ represents the capacitance of the piezoelectric transducer, and $\vartheta=-e_{31}b_p h_{pc}$ is the piezoelectric coupling term. The clamped boundary condition implies that $\frac{\partial^2 w_1\left(0,t\right)}{\partial x_1\partial t}=0$ at x_1=0. Eq.(6) thus becomes:

$$i_p(t)=\vartheta\left.\frac{\partial^2 w_1\left(x_1,t\right)}{\partial x_1\partial t}\right|_{x_1=L_1}-C_p\frac{dv(t)}{dt} \tag{7}$$

The governing equations of the electromechanical system are formed by Eq.(2) and Eq.(6). In the following, the mode shapes of this system are determined. Then, based on the calculated mode shapes, the modal superposition method is employed to derive the closed-form solution of the electromechanically coupled equations.

2.1. Modal analysis

To determine the natural frequencies and mode shapes of the beam, the damping and the coupling terms are dropped first. The governing equations of the beam are simplified to be:

$$\begin{cases} EI_1\dfrac{d^4\phi_1\left(x_1\right)}{dx_1^4}-\omega^2 m_1\phi_1\left(x_1\right)=0 \\ EI_2\dfrac{d^4\phi_2\left(x_2\right)}{dx_2^4}-\omega^2 m_2\phi_2\left(x_2\right)=0 \end{cases} \tag{8}$$

where $\phi_1\left(x_1\right)$ and $\phi_2\left(x_2\right)$ are the mode shapes of the beam sections with and without the piezoelectric layer. Their solution forms are as follows:

$$\begin{cases} \phi_1\left(x_1\right)=A_1\sin\beta_1 x_1+B_1\cos\beta_1 x_1+C_1\sinh\beta_1 x_1+D_1\cosh\beta_1 x_1 \\ \phi_2\left(x_2\right)=A_2\sin\beta_2 x_2+B_2\cos\beta_2 x_2+C_2\sinh\beta_2 x_2+D_2\cosh\beta_2 x_2 \end{cases} \tag{9}$$

in which $\beta_k^4 = \omega^2 m_k / E_k I_k$, k = 1, 2. The boundary conditions (i.e., clamped, lumped tip mass and continuities) are expressed as follows:

$$\begin{cases} \phi_1(0) = 0 \\ \phi_1'(0) = 0 \\ EI_2\phi_2''(L_2) = 0 \\ EI_2\phi_2'''(L_2) = -\omega^2 M_t \phi_2(L_2) \end{cases} \qquad \begin{cases} \phi_1(L_1) = \phi_2(0) \\ \phi_1'(L_1) = \phi_2'(0) \\ EI_1\phi_1''(L_1) = 0 \\ EI_1\phi_1'''(L_1) = EI_2\phi_2'''(0) \end{cases} \tag{10}$$

By substituting Eq.(9) into Eq.(10), simplifying and equating the determinant of the coefficient matrix to be zero for non-trivial solutions, one obtains:

$$\begin{vmatrix} (T_1N_1 + T_2N_3 + T_3N_5 + T_4N_7) & (T_1N_2 + T_2N_4 + T_3N_6 + T_4N_8) \\ (T_5N_1 + T_6N_3 + T_7N_5 + T_8N_7) & (T_5N_2 + T_6N_4 + T_7N_6 + T_8N_8) \end{vmatrix} = 0 \tag{11}$$

where

$$\begin{cases} R_1 = \dfrac{\beta_1}{\beta_2} \\ R_2 = \dfrac{E_1I_1\beta_1^2}{E_2I_2\beta_2^2} \\ R_3 = \dfrac{E_1I_1\beta_1^3}{E_2I_2\beta_2^3} \end{cases} \quad \begin{cases} N_1 = \left[(R_1 + R_3)\cos\beta_1L_1 - (R_1 - R_3)\cosh\beta_1L_1\right]/2 \\ N_2 = -\left[(R_3 + R_1)\sin\beta_1L_1 + (R_1 - R_3)\sinh\beta_1L_1\right]/2 \\ N_3 = \left[(1 + R_2)\sin\beta_1L_1 - (1 - R_2)\sinh\beta_1L_1\right]/2 \\ N_4 = \left[(1 + R_2)\cos\beta_1L_1 - (1 - R_2)\cosh\beta_1L_1\right]/2 \\ N_5 = \left[(R_1 - R_3)\cos\beta_1L_1 - (R_1 + R_3)\cosh\beta_1L_1\right]/2 \\ N_6 = \left[(R_3 - R_1)\sin\beta_1L_1 - (R_3 + R_1)\sinh\beta_1L_1\right]/2 \\ N_7 = \left[(1 - R_2)\sin\beta_1L_1 - (1 + R_2)\sinh\beta_1L_1\right]/2 \\ N_8 = \left[(1 - R_2)\cos\beta_1L_1 - (1 + R_2)\cosh\beta_1L_1\right]/2 \end{cases} \quad \begin{cases} T_1 = \left(-\sin\beta_2L_2 - \beta_2^3 I_t \cos\beta_2L_2/m_2\right) \\ T_2 = \left(-\cos\beta_2L_2 + \beta_2^3 I_t \sin\beta_2L_2/m_2\right) \\ T_3 = \left(\sinh\beta_2L_2 - \beta_2^3 I_t \cosh\beta_2L_2/m_2\right) \\ T_4 = \left(\cosh\beta_2L_2 - \beta_2^3 I_t \sinh\beta_2L_2/m_2\right) \\ T_5 = \left(-\cos\beta_2L_2 + \beta_2^3 M_t \sin\beta_2L_2/m_2\right) \\ T_6 = \left(\sin\beta_2L_2 + \beta_2^3 M_t \cos\beta_2L_2/m_2\right) \\ T_7 = \left(\cosh\beta_2L_2 + \beta_2^3 M_t \sinh\beta_2L_2/m_2\right) \\ T_8 = \left(\sinh\beta_2L_2 + \beta_2^3 M_t \cosh\beta_2L_2/m_2\right) \end{cases}$$

Solving Eq.(11) which is a polynomial equation of ω yields the natural frequencies of this cantilevered beam. The corresponding mode shapes can then be determined by substituting the calculated natural frequencies back into the boundary condition equations to seek the solutions of the coefficients of the trigonometric functions in Eq.(9).

2.2. Frequency response of voltage output

The orthogonality relations of the beam are as follows:

$$\begin{cases} \displaystyle\int_{x_1=0}^{L_1} m_1\phi_{1,j}(x_1)\phi_{1,i}(x_1)\,dx_1 + \int_{x_2=0}^{L_2} m_2\phi_{2,j}(x_2)\phi_{2,i}(x_2)\,dx_2 + M_t\phi_{2,i}(L_2)\phi_{2,j}(L_2) = \delta_{ij} \\ \displaystyle\int_{x_1=0}^{L_1} EI_1 \frac{d^4\phi_{1,i}(x_1)}{dx_1^4}\phi_{1,j}(x_1)\,dx + \int_{x_2=0}^{L_2} EI_2 \frac{d^4\phi_{2,i}(x_2)}{dx_2^4}\phi_{2,j}(x_2)\,dx_2 - EI_2\phi_{2,i}'''(L_2)\phi_{2,j}(L_2) = \omega_i^2\delta_{ij} \end{cases} \tag{12}$$

where subscripts i and j represent the i^{th} and j^{th} vibration modes. Using the modal superposition, the relative displacement along the beam can be expressed as the series of the product of mode shape functions and modal coordinates as:

$$\begin{cases} w_1\left(x_1,t\right)=\sum_{r=1}^{\infty}\phi_{1,r}\left(x_1\right)\eta_r\left(t\right) \\ w_2\left(x_2,t\right)=\sum_{r=1}^{\infty}\phi_{2,r}\left(x_2\right)\eta_r\left(t\right) \end{cases} \tag{13}$$

Substituting Eq.(13) into Eq.(2), multiplying by $\phi_{1,r}\left(x_1\right)$ and $\phi_{2,r}\left(x_2\right)$, integrating over each beam section, and then using the orthogonality relations, the modal mechanical governing equation can be obtained:

$$\frac{d^2\eta_r(t)}{dt^2}+2\zeta_r\omega_r\frac{d\eta_r(t)}{dt}+\omega_r^2\eta_r(t)+\chi_r v(t)=\gamma_r A_{cc}e^{j\omega t} \tag{14}$$

where $\chi_r=\vartheta\left.\frac{d\phi_{1,r}\left(x_1\right)}{dx_1}\right|_{x_1=L_1}$, $\gamma_r=\left\{\int_{x_1=0}^{L_1}-\phi_{1,r}\left(x_1\right)m_1dx_1+\int_{x_2=0}^{L_2}-\phi_{2,r}\left(x_2\right)\left[m_2+M_t\delta\left(x_2-L_2\right)\right]dx_2\right\}$

and A_{cc} is the amplitude of the acceleration of the base $\ddot{w}_b(t)$. In steady state, the voltage response has the form of $v(t)=V_pe^{j\omega t}$. The modal response can then be obtained as:

$$\eta_r(t)=\frac{\left(\gamma_r A_{cc}-\chi_r V_p\right)e^{j\omega t}}{\omega_r^2-\omega^2+j2\zeta_r\omega_r\omega} \tag{15}$$

The relative displacement at the free end can thus be expressed by substituting Eq.(15) into Eq.(13):

$$w_2\left(L_2,t\right)=\sum_{r=1}^{\infty}\frac{\phi_{2,r}\left(L_2\right)\left(\gamma_r A_{cc}-\chi_r V_p\right)e^{j\omega t}}{\omega_r^2-\omega^2+j2\zeta_r\omega_r\omega} \tag{16}$$

Substituting Eq.(13) into Eq.(7) yields the modal circuit governing equation:

$$C_p\frac{dv(t)}{dt}+i_p(t)=\sum_{r=1}^{\infty}\chi_r\frac{d\eta_r(t)}{dt} \tag{17}$$

Considering that the PEH is shunted to a resistive load R_{AC} implying $i_p(t)=v(t)/R_{AC}$, then combining Eq.(17) and Eq.(15), one can solve for V_p as:

$$V_p=\frac{\sum_{r=1}^{\infty}\chi_r\frac{j\omega\gamma_r A_{cc}}{\omega_r^2-\omega^2+j2\zeta_r\omega_r\omega}}{\left\{\left(\frac{1}{R_{AC}}+j\omega C_p\right)+\sum_{r=1}^{\infty}\frac{j\omega\chi_r^2}{\omega_r^2-\omega^2+j2\zeta_r\omega_r\omega}\right\}} \tag{18}$$

3. SDOF representation model

In consideration of the complexity of the derivation process and the final expression of the distributed parameter model, when the energy harvester is shunted to a complicated interface circuit, it can be anticipated that the corresponding analysis will be very difficult. To address this issue, we propose a simplified SDOF representation model of the partially covered piezoelectric energy harvester, which, to our best knowledge, has not been reported in the literature. The proposed method provides a way to model the energy harvester as a SDOF system whose equivalent lumped parameters can be directly determined from the material and geometric parameters of the energy harvester system.

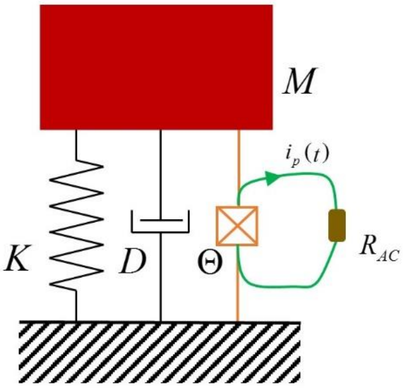

Figure 2. SDOF representation model of the partially covered cantilevered PEH.

By using the relationship between the bending moment and the beam deflection from Euler beam theory, the functions that describe the static deflections under gravity of the two beam sections with and without piezoelectric coverage are derived. For the section with piezoelectric coverage (i.e., $0 \le x_1 \le L_1$), the deflection shape, $y_1(x)$:

$$y_1(x_1)=\frac{g}{24EI_1}\left[m_1x_1^4-4(m_1L_1+m_2L_2+M_t)x_1^3+6\left(m_1L_1^2+m_2L_2(2L_1+L_2)+2M_t(L_1+L_2)\right)x_1^2\right] \quad (19)$$

where g is the gravitational constant. Combining with the continuity conditions of displacement and slope at the intersection, the deflection of the section, $y_2(x)$, without piezoelectric coverage (i.e., $0 \le x_2 \le L_2$) is:

$$y_2(x_2)=\frac{1}{24EI_2}\left[m_2gx_2^4-4(m_2L_2+M_t)gx_2^3+6\left(m_2L_2^2+M_tL_2\right)gx_2^2\right]+y_1'(L_1)x_2+y_1(L_1) \quad (20)$$

To represent the cantilevered PEH by a linear SDOF model as shown in Figure 2, the equivalent lumped parameters (i.e., the equivalent stiffness K and the equivalent mass M) are assumed to be concentrated at the free end. The following procedure determines *K* and *M*. First, the static deflection at the free end of the beam under gravity is calculated:

$$\frac{\left(M_{static}+M_t\right)g}{K}=y_2\left(L_2\right) \tag{21}$$

where M_{static} is the equivalent static mass of the beam. Also the static deflection at the free end caused by the weight of the beam only without tip mass is:

$$\frac{M_{static}g}{K}=y_2\left(L_2\right) \quad \text{at } M_t=0 \tag{22}$$

Combining Eq.(21) and (22), the equivalent stiffness of the beam can be derived:

$$K=\frac{M_t g}{y_2\left(L_2\right)-y_2\left(L_2,M_t=0\right)}=\frac{3EI_1EI_2}{EI_1L_2^3+3EI_2L_1L_2^2+3EI_2L_1^2L_2+EI_2L_1^3} \tag{23}$$

The Rayleigh’s method is used to calculate the natural frequency of the cantilevered beam without the tip mass and then the dynamic equivalent mass at the free end of the beam. The maximum potential energy *P* in the beam is:

$$P=\frac{EI_1}{2}\int_0^{L_1}\left(\frac{d^2y_1}{dx_1^2}\right)^2dx_1+\frac{EI_2}{2}\int_0^{L_2}\left(\frac{d^2y_2}{dx_2^2}\right)^2dx_2 \tag{24}$$

The maximum kinetic energy *T* in the beam is:

$$T=\frac{1}{2}\rho_1A_1\omega_n^2\int_0^{L_1}y_1^2dx_1+\frac{1}{2}\rho_2A_2\omega_n^2\int_0^{L_2}y_2^2dx_2+\frac{1}{2}M_t\omega_n^2y_2^2\left(L_2\right) \tag{25}$$

where ω_n is the natural frequency. Equating the maximum potential energy (*P*) to the maximum potential energy (*T*) yields:

$$\omega_n^2=\sum_{p=0}^{5}n_pL_1^p\Bigg/\sum_{q=0}^{9}d_qL_1^q \tag{26}$$

where

$$\begin{cases}
n_0=756EI_1^2EI_2L_2^3\left(3m_2^2L_2^2+15m_2L_2M_t+20M_t^2\right)\\
n_1=11340EI_1EI_2^2L_2^2\left(m_2L_2+2M_t\right)^2\\
n_2=22680EI_1EI_2^2L_2\left(m_2L_2+M_t\right)\left(m_2L_2+2M_t\right)\\
n_3=7560EI_1EI_2^2\left(2m_2^2L_2^2+m_1m_2L_2^2+4m_2L_2M_t+2m_1L_2M_t+2M_t^2\right)\\
n_4=11340EI_1EI_2^2m_1\left(m_2L_2+M_t\right)\\
n_5=2268EI_1EI_2^2m_1^2
\end{cases}$$

$$\begin{cases} d_0 = 2EI_1^2 L_2^6 \left(91m_2^3 L_2^3 + 819m_2^2 L_2^2 M_t + 2484m_2 L_2 M_t^2 + 2520M_t^3\right) \\ d_1 = 126EI_1 EI_2 L_2^5 \left(m_2 L_2 + 2M_t\right)\left(13m_2^2 L_2^2 + 78m_2 L_2 M_t + 120M_t^2\right) \\ d_2 = 252EI_2 L_2^4 \begin{pmatrix} 15EI_2 m_2^3 L_2^3 + 11EI_1 m_2^3 L_2^3 + 105EI_2 m_2^2 L_2^2 M_t + 77EI_1 m_2^2 L_2^2 M_t \\ +240EI_2 m_2 L_2 M_t^2 + 174EI_1 m_2 L_2 M_t^2 + 180EI_2 M_t^3 + 120EI_1 M_t^3 \end{pmatrix} \\ d_3 = 42EI_2 L_2^3 \begin{pmatrix} 315EI_2 m_2^3 L_2^3 + 36EI_1 m_2^3 L_2^3 + 13EI_1 m_1 m_2^2 L_2^3 + 1890EI_2 m_2^2 L_2^2 M_t + 216EI_1 m_2^2 L_2^2 M_t + 78EI_1 m_1 m_2 L_2^2 M_t \\ +3600EI_2 m_2 L_2 M_t^2 + 420EI_1 m_2 L_2 M_t^2 + 120EI_1 m_1 L_2 M_t^2 + 2160EI_2 M_t^3 + 240EI_1 M_t^3 \end{pmatrix} \\ d_4 = 63EI_2 L_2^2 \begin{pmatrix} 315EI_2 m_2^3 L_2^3 + 40EI_2 m_1 m_2^2 L_2^3 + 9EI_1 m_1 m_2^2 L_2^3 + 1575EI_2 m_2^2 L_2^2 M_t + 200EI_2 m_1 m_2 L_2^2 M_t \\ +45EI_1 m_1 m_2 L_2^2 M_t + 2460EI_2 m_2 L_2 M_t^2 + 240EI_2 m_1 L_2 M_t^2 + 60EI_1 m_1 L_2 M_t^2 + 1200EI_2 M_t^3 \end{pmatrix} \\ d_5 = 252EI_2^2 L_2 \left(60m_2^3 L_2^3 + 31m_1 m_2^2 L_2^3 + 240m_2^2 L_2^2 M_t + 124m_1 m_2 L_2^2 M_t + 300m_2 L_2 M_t^2 + 114m_1 L_2 M_t^2 + 120M_t^3\right) \\ d_6 = 84EI_2^2 \begin{pmatrix} 60m_2^3 L_2^3 + 117m_1 m_2^2 L_2^3 + 180m_2^2 L_2^2 M_t + 5m_1^2 m_2 L_2^3 + 351m_1 m_2 L_2^2 M_t \\ +180m_2 L_2 M_t^2 + 15m_1^2 L_2^2 M_t + 234m_1 L_2 M_t^2 + 60M_t^3 \end{pmatrix} \\ d_7 = 72EI_2^2 m_1 \left(69m_2^2 L_2^2 + 22m_1 m_2 L_2^2 + 138m_2 L_2 M_t + 44m_1 L_2 M_t + 69M_t^2\right) \\ d_8 = 1638EI_2^2 m_1^2 \left(m_2 L_2 + M_t\right) \\ d_9 = 1182EI_2^2 m_1^3 \end{cases}$$

Recall that the equivalent stiffness of the beam at the free end ha0073 been already derived in Eq.(23), the equivalent dynamic mass is thus:

$$M = M_{dynamic} = \frac{K}{\omega_n^2} \tag{27}$$

It is noteworthy that this is an electromechanical system, because of the presence of a piezoelectric transducer. Therefore, for the piezoelectric effect, one more lumped parameter is needed to be determined, i.e., the equivalent electromechanical coupling coefficient of the piezoelectric transducer. As the equivalent parameters are assumed to be located at the free end, Eq.(6) is rearranged as:

$$i_p(t) = \left[\vartheta \frac{\partial^2 w_1(x_1,t)}{\partial x_1 \partial t} \bigg|_{x_1=L_1} \frac{1}{w_2(L_2,t)} \right] w_2(L_2,t) - C_p \frac{dv(t)}{dt} \tag{28}$$

Substituting Eq.(13) into Eq.(28) and considering the first mode only yields:

$$i_p(t) = \left[\vartheta \frac{d\phi_{1,1}(x_1)}{dx_1} \bigg|_{x_1=L_1} \frac{1}{\phi_{2,1}(L_2)} \right] \phi_{2,1}(L_2) \frac{d\eta_1(t)}{dt} - C_p \frac{dv(t)}{dt} \tag{29}$$

$\phi_{2,1}(L_2)\, d\eta_1(t)/dt$ is actually the velocity of the beam at the free end, i.e., $dw(L_2,t)/dt$. The equivalent electromechanical coupling coefficient is obtained as:

$$\Theta = \vartheta \frac{d\phi_{1,1}(x_1)}{dx_1}\bigg|_{x_1=L_1} \frac{1}{\phi_{2,1}(L_2)} \tag{30}$$

By using the derived static deflection function (i.e., Eqs.(19) and (20)) to approximate the first mode shape function of the beam, the equivalent electromechanical coupling coefficient can be expressed as:

$$\Theta = \frac{4EI_2L_1^3m_1 + 12EI_2L_1L_2(L_1+L_2)m_2 + 12EI_2L_1(L_1+2L_2)M_t}{\left\{\begin{array}{l} EI_2L_1^3(3L_1+4L_2)m_1 + \left[3EI_1L_2^4 + EI_2L_1L_2\left(12L_2^2+18L_1L_2+8L_1^2\right)\right]m_2 \\ +8\left[EI_1\left(L_1^3+L_2^3\right)+3EI_2L_1L_2(L_1+L_2)\right]M_t \end{array}\right\}} \tag{31}$$

Therefore, the dynamic behavior of the cantilevered PEH with partial piezoelectric coverage can be equivalently represented by the SDOF model. The governing equations can be expressed as:

$$\begin{cases} M\ddot{u}(t) + D\dot{u}(t) + Ku(t) + \Theta v(t) = -M\ddot{w}_b(t) \\ \dfrac{v(t)}{R_{AC}} + C_p\dot{v}(t) - \Theta\dot{u}(t) = 0 \end{cases} \tag{32}$$

where $D = 2\zeta M\omega_n$ is the damping coefficient that can be calculated according to the damping ratio ζ of the continuous system, and R_{AC} is the resistive load connected to the piezoelectric transducer. The displacement at the free end $w_2(L_2,t)$ is redefined as u for brevity. Another way to convert Eqs.(14) and (17) into the lumped form around the fundamental natural frequency as Eq.(32) is dividing Eq.(14) by $\phi_{2,1}(L_2)$, followed by rearranging using a variable substitution $u(t) = \phi_{2,1}(L_2)\eta_1(t)$. This leads to the equivalent lumped parameters as follows.

$$\begin{array}{ll} M = \dfrac{1}{\phi_{2,1}^2(L_2)} & K = \dfrac{\omega_1^2}{\phi_{2,1}^2(L_2)} \\ D = \dfrac{2\zeta_1\omega_1}{\phi_{2,1}^2(L_2)} & \Theta = \dfrac{\chi_1}{\phi_{2,1}(L_2)} \end{array} \tag{33}$$

The reason for not preferring to derive the equivalent lumped parameters by this means is that these are mode shape dependent, thus the final expressions are comparatively complicated and implicit. For the lumped parameter model described by Eq.(32), one can easily obtain the expression of the relative displacement as:

$$u(t)=\frac{A_{cc}-\frac{\Theta}{M}V_p}{\omega_1^2-\omega^2+j2\zeta_1\omega_1\omega}e^{j\omega t} \tag{34}$$

From the analytical solution of the distributed parameter model, by neglecting contributions from higher modes, Eq.(16) becomes:

$$w_2\left(L_2,t\right)=\frac{\phi_{2,1}\left(L_2\right)\gamma_1 A_{cc}-\phi_{2,1}\left(L_2\right)\chi_1 V_p}{\omega_1^2-\omega^2+j2\zeta_1\omega_1\omega}e^{j\omega t} \tag{35}$$

Note that from Eq.(33), one obtains the relation equation $\Theta/M=\phi_{2,1}\left(L_2\right)\chi_1$. Then, based on the comparison between Eqs.(34) and (35), it is found that a correction factor μ should be introduced to the forcing term A_{cc} to improve the prediction based on the SDOF model as given below.

$$\mu=\phi_{2,1}\left(L_2\right)\gamma_1=\phi_{2,1}\left(L_2\right)\left\{\int_{x_1=0}^{L_1}\phi_{1,r}\left(x_1\right)m_1dx_1+\int_{x_2=0}^{L_2}\phi_{2,r}\left(x_2\right)m_2dx_2+\phi_{2,r}\left(L_2\right)M_t\right\} \tag{36}$$

The analytical mode shape function of the beam with a varying cross-section is difficult to calculate. Therefore, to simplify the calculation of μ, the derived static deflection functions Eq.(19) and Eq.(20) are used to approximate the exact first mode shape. The correction factor μ can thus be derived in the explicit form as:

$$\mu=\frac{\omega_n^2}{24EI_1EI_2}\left[\begin{array}{l}\left(4L_2+3L_1\right)EI_2L_1^3m_1+\left(3\frac{EI_1}{EI_2}L_2^3+12L_1L_2^2+18L_1^2L_2+8L_1^3\right)EI_2L_2m_2\\+\left(8\frac{EI_1}{EI_2}L_2^3+24L_1L_2^2+24L_1^2L_2+8L_1^3\right)EI_2M_t\end{array}\right] \tag{37}$$

The forcing term in Eq.(32) should be corrected by multiplying with μ, and the resultant governing equations of the electromechanical system become:

$$\begin{cases}M\ddot{u}(t)+D\dot{u}(t)+Ku(t)+\Theta v(t)=-\mu M\ddot{w}_b(t)\\ \dfrac{v(t)}{R_{AC}}+C_p\dot{v}(t)-\Theta\dot{u}(t)=0\end{cases} \tag{38}$$

Indeed, this electromechanical system has an additional electrical degree-of-freedom (DOF) *v*(*t*). Throughout this paper, it is simply referred to as a SDOF system as this system has only one mechanical DOF.

4. Comparison of SDOF and distributed parameter models

In this section, frequency domain analyses are performed to investigate the voltage responses of the developed SDOF representation model. A constant acceleration field of A_{cc}= -1 m/s^2 is applied onto the system. The resistance load is set to be $10^{12}\Omega$, i.e., the circuit connection can be regarded as an open-circuit condition. The system damping ratio ζ is assumed to be 0.008. Comparisons between the developed SDOF model and the distributed parameter model (analytical model) are then presented to verify the proposed equivalent SDOF representation. The results of the uncorrected SDOF model, i.e., without using the correction factor, are also provided to clearly demonstrate the improvements brought by the introduction of the correction factor. The geometric and material parameters of the system used in the following case studies are listed in Table 1.

Table 1. Geometric and material parameters of the system under investigation.

Parameters	**Values**	**Materials**	**Parameters**	**Values**
Substrate beam length	62.5 mm	Steel	Mass density	7850 kg/m^3
Substrate beam width	10 mm		Young's Modulus	200 GPa
Substrate beam thickness	1 mm	PZT-5A	Mass density	7800 kg/m^3
Piezoelectric layer length	28 mm		Young's Modulus	66 GPa
Piezoelectric layer width	8 mm		e_{31}	-12.5 C/m^2
Piezoelectric layer thickness	0.2 mm		ε_{33}	1.3281×10^{-8} F/m

Since the utilization of the vibration mode approximated by the static deflection plays a significant role in the development of the SDOF representation, the analytical and the static-deflection approximated vibration modes are firstly compared to confirm the rationality of this approximation treatment. For different tip mass M_t, Figure 3 compares the fundamental vibration modes obtained from the static-deflection approximation, the analytical method and the finite element (FE) simulation by using the commercial software ANSYS. The absolute errors of the static-deflection approximated mode shape as compared with the analytical solution and the FE simulation result are also provided. It is worth mentioning that the errors should refer to the right side y-axis. It can been seen that the solid line which denotes the approximated result, the dash-dot line which denotes the analytical result and the dotted line which denotes the FE result almost coincide with each other. The absolute errors of the approximated vibration modes are very small. The discontinuities in the error curves appear at the position corresponds to the interface between the sections with and without piezoelectric coverages. In addition, by comparing Figure 3(a) to (d), it can be noted that with an increase of M_t, the absolute error decreases, which means that the accuracy of the approximated vibration mode increases. Moreover, the absolute error of the approximated vibration mode is extremely small as compared with the analytical result for the cases when M_t is relatively large (Figure 3(b), (c) and (d)). Therefore, it is reasonable to use the static deflection to approximate the fundamental vibration mode of the cantilevered energy harvester.

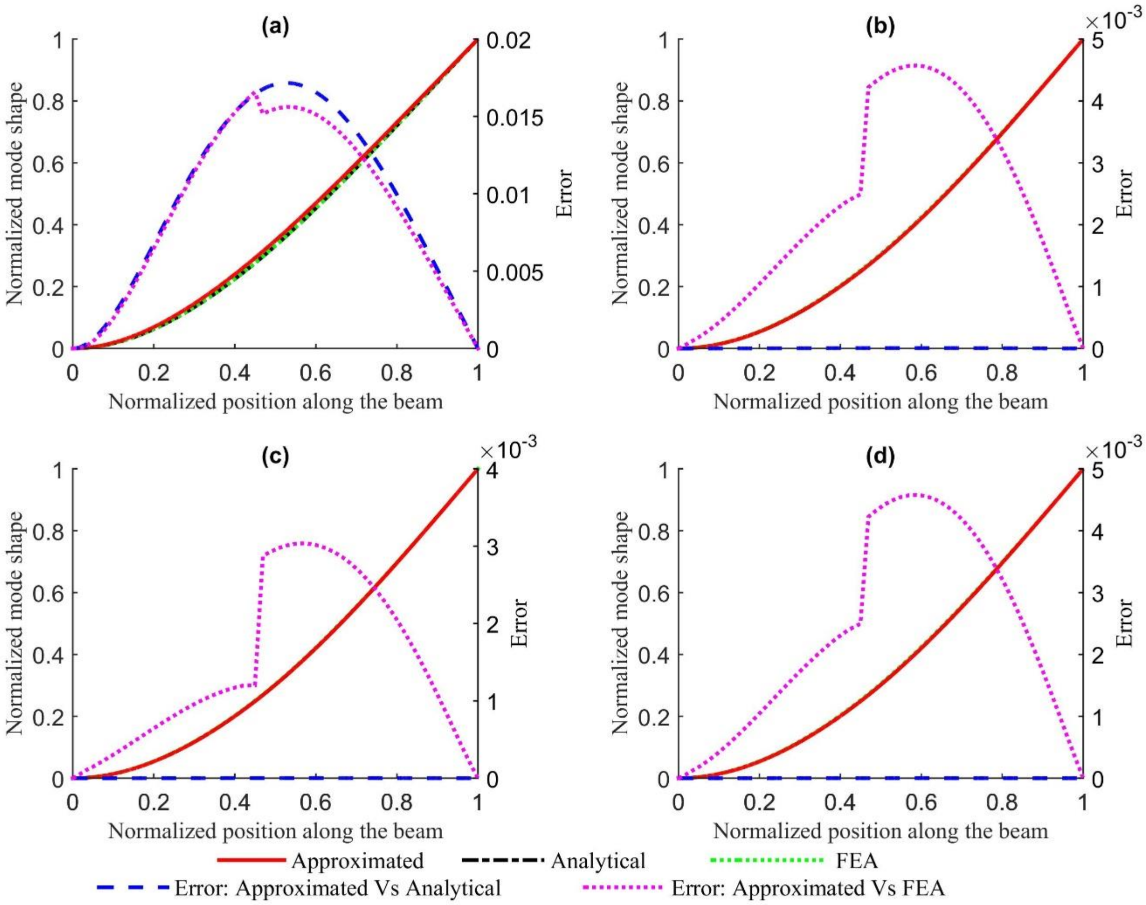

Figure 3. Comparisons of the fundamental vibration modes approximated by the static deflection and predicted by the analytical method and FEA: (a) M_t=0 g; (b) M_t =10 g; (c) M_t =20 g; (d) M_t =30 g.

Figure 4 shows the voltage responses of the corrected SDOF, uncorrected SDOF, FE and distributed parameter models for the cases with different tip masses. For the analytical results derived by the mode superposition method, three modes are used in the calculation.

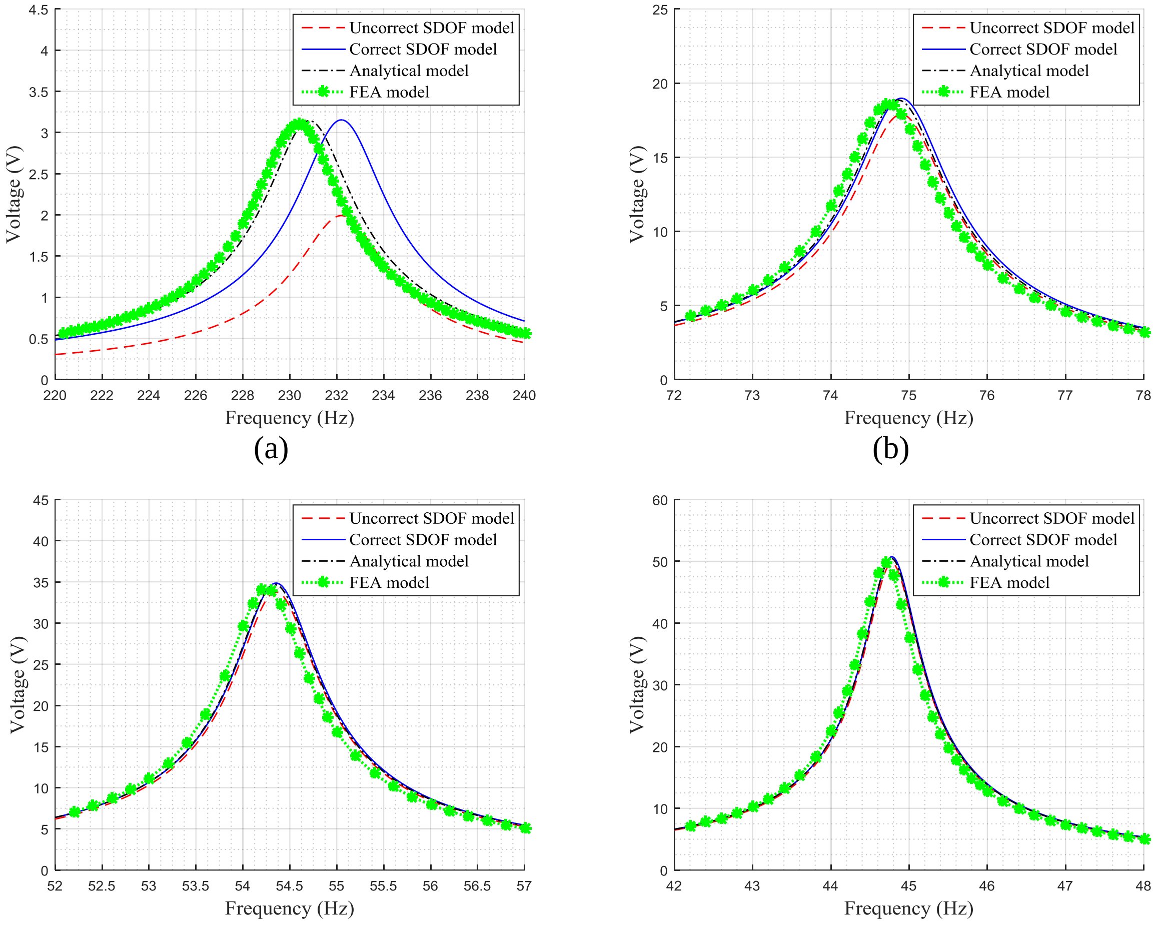

(a) (b)

(c) (d)

Figure 4. Comparisons between the voltage responses of the uncorrected SDOF, corrected SDOF, analytical and FEA models: (a) M_t=0 g; (b) M_t =10 g; (c) M_t =20 g; (d) M_t =30 g.

From Figure 4(a) corresponding to the case of M_t = 0 g (i.e., no tip mass), both the uncorrected and corrected SDOF models yield the same prediction of the fundamental natural frequency as 232.2 Hz which is slightly different from the predication of the distributed parameter model (230.8 Hz) and that of the FE model (230.4 Hz). So the relative error for the approximately predicted natural frequency is 0.61% as compared with the analytical result. This shows both the SDOF models provide a good estimation of the fundamental natural frequency. However, in terms of the voltage amplitude response, the peak value in the voltage response of the uncorrected SDOF model is about 1.99 V and the actual values from the analytical and the FE models are 3.14 V and 3.10 V, respectively. The relative error in the prediction of the voltage amplitude based on the uncorrected SDOF model is 36.62% with respect to the analytical model. The peak value of voltage for the corrected SDOF model is about 3.15 V which indicates only a 0.32% relative error as compared to the distributed parameter model. It can be found that for the case where there is no tip mass, the accuracy of the SDOF representation is significantly increased after the introduction of the correction factor.

Figure 4(b)-(d) shows a few more cases of different tip mass M_t. For the corrected SDOF model, it can be found that in terms of both the fundamental natural frequency and the voltage amplitude response, the voltage estimations with sufficient accuracy can always be ensured. For the uncorrected SDOF model, it can be noted that with an increase of M_t, the relative predictive accuracy increase (i.e., the errors decrease). Among these four cases, even when M_t is increased to 30 g (Figure 4(d)) a slight difference between the results from the uncorrected SDOF model and the distributed parameter model is still noticed. This implies that the uncorrected SDOF model is suitable for use in the case where the tip mass is relatively large.

To further reveal the effects of M_t on the prediction accuracy of the SDOF model, Figure 5 shows the relative errors of several parameters (i.e., μ, Θ and ω_n) for different α which is the ratio of M_t to the mass of the entire beam at static condition. Recalling that the correction factor μ, the lumped electromechanical coefficient Θ and the fundamental natural frequency ω_n can be determined approximately both using static deflection and analytically using the distributed parameter model. By treating the values from the distributed parameter model as the actual ones, Figure 5(a) shows the relative errors of the approximately determined values of μ, Θ and ω_n for different values of M_t. It can be noted that with an increase of M_t, the relative error of ω_n decreases. Although the relative errors of μ and Θ first increase then decrease, the overall trends can be considered as decreasing. Since the estimations of all these three parameters based on the SDOF model become more accurate with an increase of M_t, it can be anticipated that the prediction accuracy in terms of the maximum voltage amplitude should also increase. This is also reflected in Figure 5(b). The solid line and the dash-dot lines denote the relative errors of the corrected SDOF model and the uncorrected model, respectively. In addition, it is noteworthy that the data of the uncorrected SDOF model refers to the right-side *y*-axis, since the relative error of the uncorrected model is larger than that of the corrected SDOF model by several orders of magnitude. Figure 5(b) shows the effect of M_t on the SDOF model in the prediction of the maximum voltage amplitude. With the increase of M_t, the overall trends of the relative errors of the predicted maximum voltage amplitude are decreasing which means that the prediction accuracies of the maximum voltage amplitude increase. At small α (i.e, M_t), the relative error of the uncorrected SDOF model is quite large for practical use. At $\alpha = 10$, the relative error of the uncorrected SDOF model is reduced to 0.79%, which, however, is still larger than the maximum relative error of the corrected SDOF model (0.72%). Compared to Figure 5(a), a notable phenomenon observed in the corrected SDOF model is that although the relative errors of μ , Θ and ω_n are relatively large for the case when the tip mass is near zero, the same fact does not hold for the relative prediction error of the maximum voltage amplitude. Contrary to the expectation, when M_t is relatively small, the prediction of the maximum voltage of the corrected SDOF model turns out to be accurate. This is because the relative errors of μ and Θ are of opposite nature which leads to an improved relative accuracy. Indeed, the underestimation of μ and overestimation of Θ balance out, leading to a significant reduction of the error in the maximum voltage amplitude. Since the maximum relative error of the corrected SDOF model in the prediction of the maximum voltage amplitude is $\approx$0.72% when $\alpha \approx 1$, one can conclude that the corrected SDOF model can always provide sufficient accuracy.

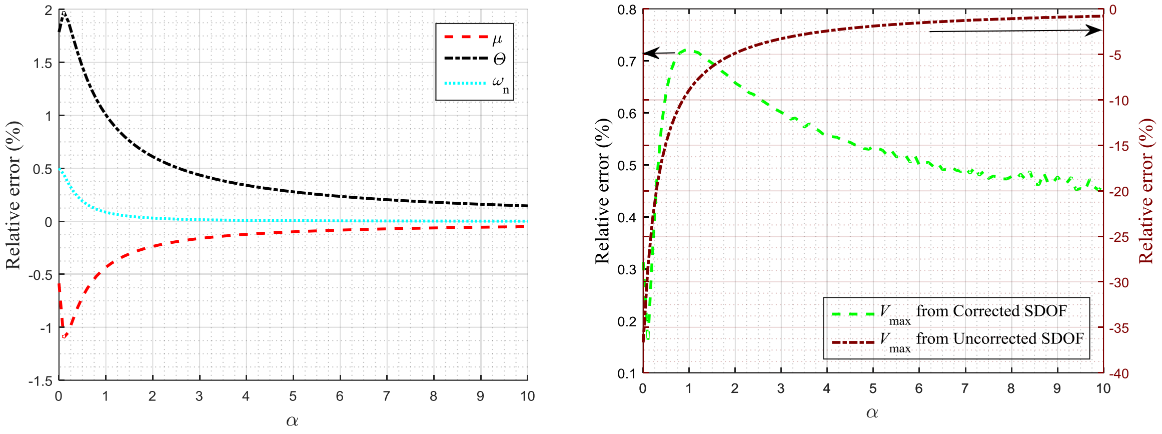

(a) (b)

Figure 5. Comparison between the approximately obtained values and analytically determined values: (a) relative errors of correction factor μ , electromechanical coupling coefficient Θ and natural frequency ω_n , (b) relative errors of maximum voltage amplitudes of corrected and uncorrected SDOF models.

5. Energy harvesting interface circuits

In this section, the practical interface circuits are taken into consideration. The cantilevered PEH is connected to a standard energy harvesting (SEH) circuit, i.e., the AC-to-DC full-wave bridge rectifier and a parallel synchronized switch harvesting on inductor (P-SSHI) circuit. In the modelling of these circuits, Shu's method (Shu et al., 2006; Shu et al., 2007) provides the analytical expressions of the power and the rectified voltage, but does not offer waveform information about the response. In addition, as aforementioned, the EIM method (Liang et al., 2012) provides a clearer view of the energy flow in the energy harvester system. It uses the first-order harmonic to approximate the waveform of the response. By including higher-order harmonic components in the calculation of the EIM method, it has the potential to reduce the distortion in the waveform response and give a more accurate waveform solution. However, the final expression of the harvested power in the EIM method is a function of the rectifier block angle which cannot be analytically determined and thus cannot calculate the rectified voltage and give the explicit expression of power in terms of load resistance. An improved EIM method is therefore required to tackle this drawback.

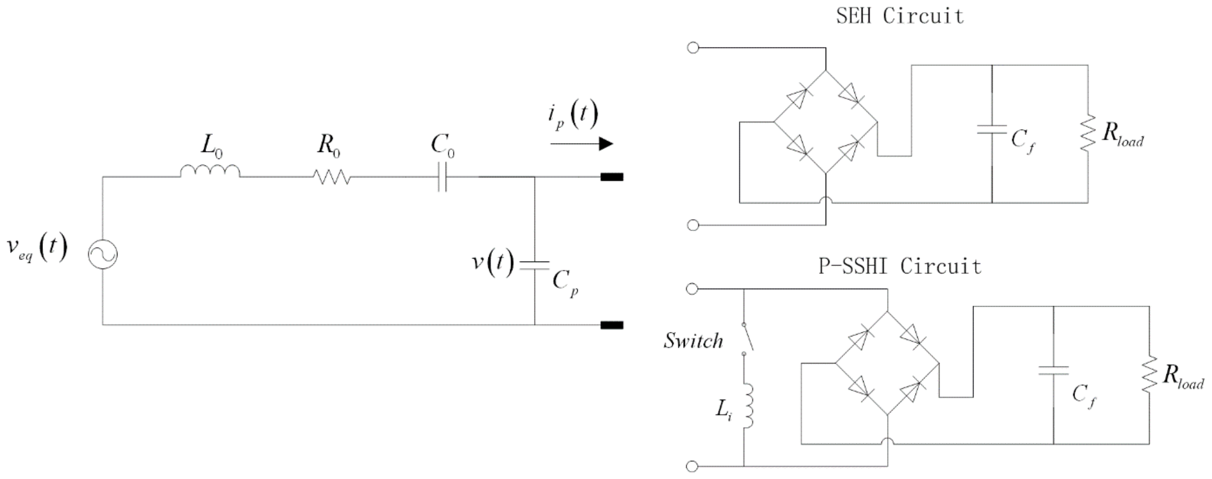

Figure 6. Equivalent circuit representation of a SDOF PEH shunted to sophisticated harvesting interface circuits.

Figure 6 shows the schematic of the equivalent circuit representation of the SDOF PEH shunted to the sophisticated harvesting circuit. For the given parameters listed in Table 1 and M_t = 30 g, the equivalent parameters of the SDOF PEH model are calculated as M = 31.1 g, K = 2407.5 N/m, D = 0.1385 Ns/m, μ = 1.022, Θ = 9.25×10^{-4} N/V and C_p = 14.9 pF. By using the mechanical-electrical analogies, the mechanical part is equivalent to an electrical model. The mechanical parameters are correspondingly converted into the electrical parameters using the following relationships.

$$\begin{cases} L_0 = M/\Theta^2 & v_{eq}(t) = -\mu M\ddot{w}_b(t)/\Theta \\ R_0 = D/\Theta^2 & i_{eq}(t) = \Theta\dot{u}(t) \\ C_0 = \Theta^2/K & \end{cases} \tag{39}$$

5.1. Analysis of SEH interface circuit

Due to the existence of the full-wave rectifier bridge, the system possesses nonlinearity. The characteristic waveform of the voltage across the DC resistance load is not harmonic anymore. By using the equivalent impedance modelling method which decomposes the voltage response into harmonic components and only considers the fundamental one, the equivalent impedance of the SEH interface circuit can be obtained as (Liang et al., 2012):

$$Z_{SEH} = \frac{1}{\pi\omega C_p}\left[\sin^2\varphi + j\left(\sin\varphi\cos\varphi - \varphi\right)\right] \tag{40}$$

where φ is the rectifier blocked angle in a half cycle and is related to the rectified voltage V_{rect} by:

$$\cos\varphi = 1 - 2\frac{V_{rect}}{V_{oc}} \tag{41}$$

where V_{oc} is the magnitude of the open-circuit voltage that is related to the displacement amplitude by:

$$V_{oc} = \frac{\Theta U}{C_p} \tag{42}$$

From Eq.(40), it is noted that the resistance and the reactance corresponding to the real component R_h and imaginary component X_E of the equivalent impedance for the SEH interface circuit are given by:

$$\begin{cases} R_h = \dfrac{1}{\pi\omega C_p}\sin^2\varphi \\ X_E = \dfrac{1}{\pi\omega C_p}\left(\sin\varphi\cos\varphi - \varphi\right) \end{cases} \tag{43}$$

It is known that the imaginary component (i.e., reactance) stores and releases energy periodically, and does not dissipate energy. Only the real component (i.e., resistance) of the equivalent impedance absorbs the energy from the source, i.e., converts mechanical energy into electric energy. Assuming that the full-wave rectifier bridge can realize the ideal AC-to-DC conversion and does not dissipate any energy, the harvested power by the SEH circuit is then equal to the energy dissipated by R_h and can be evaluated by using the following equation.

$$P_h = \frac{V_{eq}^2}{2}\frac{R_h}{\left(X_{L_0} + X_{C_0} + X_E\right)^2 + \left(R_0 + R_d + R_h\right)^2} \tag{44}$$

where $X_{L_0} = \omega L_0$ and $X_{C_0} = -1/\left(\omega C_0\right)$ are the reactance of L_0 and C_0, respectively. R_d is the dissipative component that is composed of the rectifier dissipation. Since it is assumed that the rectifier bridge can ideally perform the AC-to-DC conversion with no dissipative component, R_d equals to zero. When the system is in steady state which implies that the variation of the charge stored in the filtering capacitance is null over a cycle, by considering the balance of the charge flowing through the DC load, V_{rect} can be expressed by the amplitude of the displacement U as:

$$V_{rect} = \frac{2\omega\Theta R_{load}}{2\omega R_{load}C_p + \pi}U \tag{45}$$

Combining Eq.(45) and Eq.(42) gives:

$$\frac{V_{rect}}{V_{oc}} = \frac{2\omega R_{load}C_p}{2\omega R_{load}C_p + \pi} \tag{46}$$

Substituting Eq.(46) into Eq.(41), one obtains the equation for calculating the rectifier block angle from the DC resistance load R_{load}.

$$\varphi = \arccos\left(\frac{-2\omega R_{load}C_p + \pi}{2\omega R_{load}C_p + \pi}\right) \tag{47}$$

The expression of the harvested power of the SEH interface circuit is then obtained by substituting Eq.(43) into Eq.(44).

$$P_h = \frac{4R_{load}\left(\frac{\mu M A_{cc}}{\Theta}\right)^2}{\left(2\omega R_{load}C_p + \pi\right)^2\left[\left(\omega\frac{M}{\Theta^2} - \frac{K}{\omega\Theta^2} + \frac{1}{\pi\omega C_p}\left(\sin\varphi\cos\varphi - \varphi\right)\right)^2 + \left(\frac{D}{\Theta^2} + \frac{8R_{load}}{\left(2\omega R_{load}C_p + \pi\right)^2}\right)^2\right]} \tag{48}$$

As the rectified voltage V_{rect} is constant under steady-state operation and has the relationship with the harvested energy as $P_h = V_{rect}^2 / R_{load}$, the rectified voltage can thus be calculated:

$$V_{rect} = \sqrt{P_h R_{load}} \tag{49}$$

Shu et al. (2006) analysed the same interface circuit based on the principle of energy balance and derived the expression of the rectified voltage. Incorporating the consideration of the correction factor, the expression of V_{rect} from (Shu et al., 2006) should be rewritten as follows:

$$V_{rect} = \left(\frac{2\omega\Theta R_{load}}{2\omega C_p R_{load} + \pi} \right) \frac{\mu M A_{cc}}{\left[\left(D\omega + \frac{8\omega R_{load}\Theta^2}{\left(2\omega R_{load} C_p + \pi\right)^2} \right)^2 + \left(K - \omega^2 M + \frac{2\omega R_{load}\Theta^2}{\left(2\omega R_{load} C_p + \pi\right)} \right)^2 \right]^{\frac{1}{2}}} \tag{50}$$

The harvested power can then be calculated by using Eq.(51).

$$P_h = \frac{4R_{load} \left(\frac{\mu M A_{cc}}{\Theta} \right)^2}{\left(2\omega R_{load} C_p + \pi\right)^2 \left[\left(\frac{K}{\omega\Theta^2} - \omega \frac{M}{\Theta^2} + \frac{2R_{load}}{\left(2\omega R_{load} C_p + \pi\right)} \right)^2 + \left(\frac{D}{\Theta^2} + \frac{8R_{load}}{\left(2\omega R_{load} C_p + \pi\right)^2} \right)^2 \right]} \tag{51}$$

The modified EIM method for the SEH interface circuit will be verified by comparing the result with that from Eqs.(50) and (51), given by Shu et al. (2006).

5.2. Analysis of P-SSHI interface circuit

In the similar way, the equivalent impedance of the electrical part of the P-SSHI interface circuit can be written as (Liang et al., 2012):

$$Z_{P-SSHI} = \frac{1}{\pi\omega C_p} \left[\left(1 - \cos\varphi\right) \left(\frac{4}{1+\gamma} - 1 + \cos\varphi \right) + j\left(\sin\varphi\cos\varphi - \varphi\right) \right] \tag{52}$$

where γ is the voltage inversion factor that is related to the quality factor Q due to the energy loss, mainly from the inductor in series with the switch by $\gamma = -e^{-\pi/(2Q)}$; φ is the rectifier blocked angle in a half cycle and is related to the rectified voltage V_{rect} by:

$$\cos\varphi = 1 - \left(1 + \gamma\right) \frac{V_{rect}}{V_{oc}} \tag{53}$$

The relationship between the open-circuit voltage V_{oc} and the displacement amplitude U described by Eq.(42) still holds for the P-SSHI interface circuit. The real and imaginary components of the equivalent impedance of the P-SSHI interface circuit are:

$$\begin{cases} R_d = \dfrac{1}{\pi\omega C_p} \left(1 - \cos\varphi\right)^2 \left(\dfrac{1-\gamma}{1+\gamma} \right) \\ R_h = \dfrac{1}{\pi\omega C_p} \left(1 - \cos\varphi\right) \left(\dfrac{4}{1+\gamma} - 1 + \cos\varphi \right) \\ X_E = \dfrac{1}{\pi\omega C_p} \left(\sin\varphi\cos\varphi - \varphi\right) \end{cases} \tag{54}$$

For the same reason as explained for the SEH interface circuit, the energy dissipated by R_h represents the energy harvested by the P-SSHI interface circuit. The harvested power can be evaluated by using Eq.(44). From the perspective of the balance of the charge flowing through the DC resistance load, one can find the relationship between the rectified voltage of the P-SSHI interface circuit and the amplitude of the displacement as:

$$V_{rect} = \frac{2\omega\Theta R_{load}}{(1+\gamma)\omega R_{load}C_p + \pi}U \tag{55}$$

Combining Eq.(55) and Eq.(42) yields:

$$\frac{V_{rect}}{V_{oc}} = \frac{2\omega R_{load}C_p}{(1+\gamma)\omega R_{load}C_p + \pi} \tag{56}$$

Substituting Eq.(56) into Eq.(53) gives the expression of the rectifier blocked angle in a half cycle for the P-SSHI interface circuit:

$$\varphi = \arccos\left(\frac{-(1+\gamma)\omega R_{load}C_p + \pi}{(1+\gamma)\omega R_{load}C_p + \pi}\right) \tag{57}$$

The harvested power of the P-SSHI interface circuit is evaluated by substituting Eq.(54) into Eq.(44):

$$P_h = \frac{\dfrac{4R_{load}}{\left[(1+\gamma)\omega R_{load}C_p + \pi\right]^2}\left(\dfrac{\mu M A_{cc}}{\Theta}\right)^2}{\left(\omega\dfrac{M}{\Theta^2} - \dfrac{K}{\omega\Theta^2} + \dfrac{1}{\pi\omega C_p}(\sin\varphi\cos\varphi - \varphi)\right)^2 + \left(\dfrac{D}{\Theta^2} + \dfrac{4(1-\gamma^2)\omega R_{load}^2 C_p}{\pi\left[(1+\gamma)\omega R_{load}C_p + \pi\right]^2} + \dfrac{8R_{load}}{\left[(1+\gamma)\omega R_{load}C_p + \pi\right]^2}\right)^2} \tag{58}$$

For the P-SSHI interface circuit, the relationship between the rectified voltage and the harvested power is still the same as that for the SEH interface circuit; so Eq.(49) is still applicable for calculating the rectified voltage of the P-SSHI interface circuit. Shu et al. (2007) also developed a method for analysing the same P-SSHI interface circuit. Due to the existence of the correction factor from the mechanical domain that acts on the forcing term, the expression in (Shu et al., 2007) should be slightly modified as follows:

$$V_{rect} = \frac{\left(\dfrac{2\omega\Theta R_{load}}{(1+\gamma)\omega C_p R_{load} + \pi}\right)\mu M A_{cc}}{\left\{\left[\omega D + \dfrac{8\left(1 + \dfrac{\omega C_p R_{load}}{2\pi}(1-\gamma^2)\right)\omega\Theta^2 R_{load}}{\left((1+\gamma)\omega C_p R_{load} + \pi\right)^2}\right]^2 + \left[K - \omega^2 M + \dfrac{(1+\gamma)\omega\Theta R_{load}}{(1+\gamma)C_p\omega R_{load} + \pi}\right]^2\right\}^{\frac{1}{2}}} \tag{59}$$

The harvested power can then be obtained by using Eq.(60).

$$P_h = \frac{\dfrac{4R_{load}}{\left[(1+\gamma)\omega R_{load}C_p+\pi\right]^2}\left(\dfrac{\mu M A_{cc}}{\Theta}\right)^2}{\left(\dfrac{K}{\omega\Theta^2}-\omega\dfrac{M}{\Theta^2}+\dfrac{(1+\gamma)R_{load}}{\Theta\left[(1+\gamma)\omega R_{load}C_p+\pi\right]}\right)^2+\left(\dfrac{D}{\Theta^2}+\dfrac{4(1-\gamma^2)\omega R_{load}^2 C_p}{\pi\left[(1+\gamma)\omega R_{load}C_p+\pi\right]^2}+\dfrac{8R_{load}}{\left[(1+\gamma)\omega R_{load}C_p+\pi\right]^2}\right)^2} \quad (60)$$

The modified EIM method for the P-SSHI interface circuit will be verified by comparing the present results with those from Eqs.(59) and (60) given by Shu et al. (2007).

6. Verification of Modified EIM method

The mechanical part of the cantilevered PEH has already been represented by the developed SDOF model and converted into an equivalent circuit model. The SEH and P-SSHI interface circuits have been also converted to equivalent AC electrical components by using the modified EIM method. The energy harvesting performance of this system can then be evaluated. The results obtained by using the methods proposed by Shu et al. (2006); (Shu et al., 2007) are also provided for comparison.

6.1. *Results for SEH interface circuit*

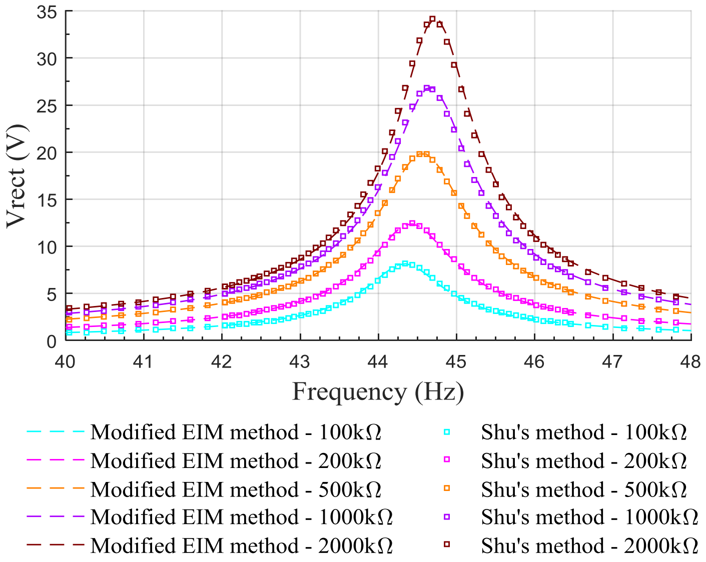

Figure 7. Frequency responses of V_{rect} for the SEH interface circuit from the modified EIM method and Shu's method (Shu et al., 2006).

Figure 7 shows the frequency responses of the rectified voltage for the case when the PEH is shunted to the SEH interface circuit. It can be seen that the results from the modified EIM method agree well with those from the Shu's method (Shu et al., 2006), which has already been validated both numerically and experimentally. For a further quantitative comparison,

Figure 8 shows the relative error of the result obtained from the modified EIM method as compared to that from the Shu's method (Shu et al., 2006). It can be observed that the relative errors are very small and negligible. In particular, the relative error becomes extremely small near the resonance frequency. This establishes the estimation accuracy of the modified EIM method to reach a higher degree near the resonance frequency.

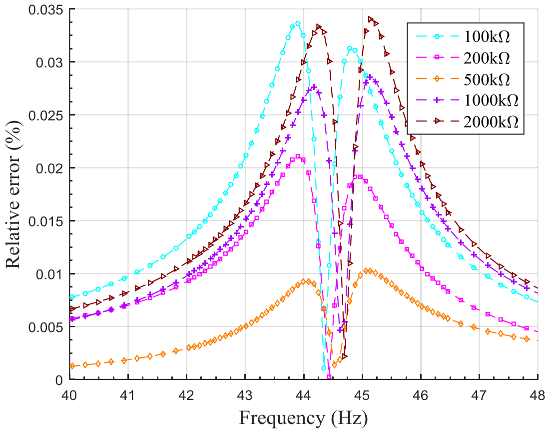

Figure 8. Relative error of V_{rect} for the modified EIM method as compared with the Shu's method (Shu et al., 2006).

Based on the finding from the frequency response of V_{rect}, one can expect that the optimal output power of the SEH interface circuit from both methods should also be in a good agreement, which is confirmed in Figure 9(a). It can be observed that in the vicinity of the resonance frequency, the predictions by both methods are very close; while farther away from the resonance frequency, the result of the modified EIM method deviates from that of the Shu's method (Shu et al., 2006). In general, the modified EIM method demonstrates a satisfying level of accuracy.

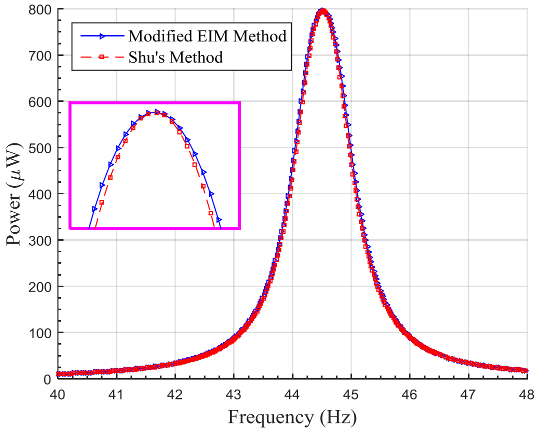

Figure 9. Optimal output power from the SEH interface circuit predicted by the modified EIM method and the Shu's method (Shu et al., 2006).

6.2. Results for P-SSHI interface circuit

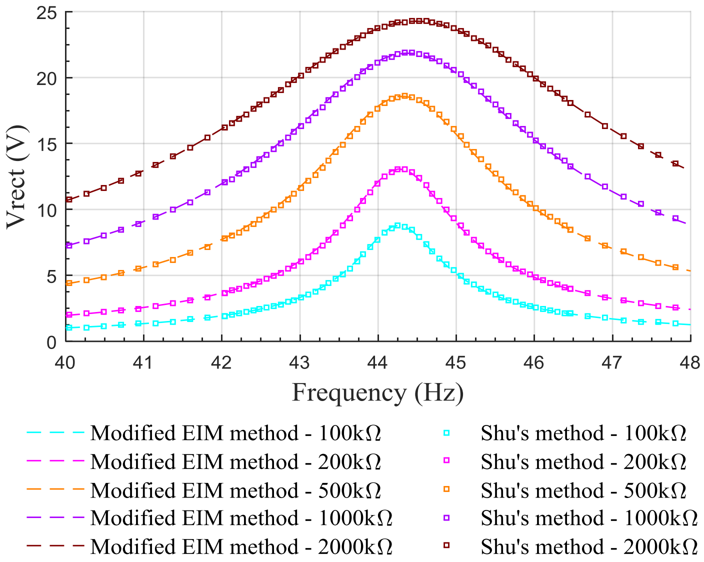

Figure 10. Frequency responses of V_{rect} for the P-SSHI interface circuit from the modified EIM method and the Shu's method (Shu et al., 2007).

Figure 10 shows the frequency responses of the rectified voltage for the case when the PEH is shunted to the P-SSHI interface circuit. The same conclusion is found to be still valid. The results from both the modified EIM method and the Shu's method (Shu et al., 2007) are very close. The relative error of the result from the modified EIM method presented in Figure 11 further confirms that the relative errors are negligible. Moreover, for the P-SSHI interface circuit, the same phenomenon is also observed in Figure 11. Around the resonance frequency, the relative errors of the predictions for the rectified voltage from the modified EIM method are extremely small. This is a useful finding as the performance around the resonance frequency is usually of most interest.

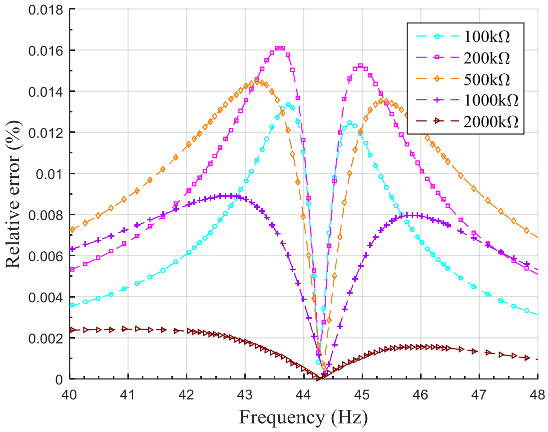

Figure 11. Relative error of V_{rect} for the modified EIM method as compared to the Shu's method (Shu et al., 2007).

Furthermore, the optimal power output responses obtained from both the methods are presented and compared in Figure 12. As expected, the solid and dash curves that denote the data from the modified EIM method and the Shu's method (Shu et al., 2007) almost coincide with each other, indicating a very good agreement. The predictions from both the methods tally with each other the best near the resonance frequency. Since the Shu's method has already been validated through numerical simulations (Shu et al., 2007), we can conclude that the results from the modified EIM method are also accurate and reliable.

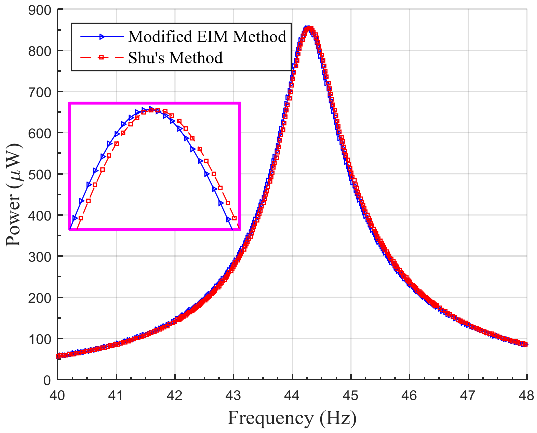

Figure 12. Optimal output power from the P-SSHI interface circuit predicted by the modified EIM method and the Shu's method (Shu et al., 2007).

7. Conclusions

In this paper, we propose a modelling methodology for a partially covered cantilevered PEH shunted to SEH and P-SSHI interface circuits. In the mechanical domain, a SDOF representation model is proposed to describe the dynamic behaviour of the system. The electromechanical coupling effect is also included into consideration, and the equivalent electromechanical coupling coefficient is expressed in an explicit form by using the static-deflection approximated fundamental vibration mode. Based on the comparison between the relative displacement transmittances at the free end of the distributed parameter model and the SDOF model, a correction factor is proposed to modify the SDOF model for improving the accuracy. The corrected SDOF model is verified through the comparison with the distributed parameter model and the finite element model. In the electrical domain, a modified EIM method is proposed for the analysis of the SEH and P-SSHI circuits. The improved EIM method provides the explicit analytical expression of the harvested power in terms of the load resistance rather than the rectifier block angle (which cannot be determined analytically in the conventional EIM method). The interface circuits are converted into equivalent AC electrical components (EIM method), which are then connected with the equivalent circuit representation of the corrected SDOF mechanical model. The energy harvesting performance is then evaluated. A good agreement between the results of the modified EIM method and the Shu's methods is observed. The combination of the developed SDOF representation model and the improved EIM method enable the mechanical and the electrical parts of the PEH system to be bridged easily. Therefore, the methods developed in this work provide an efficient and accurate tool for the future design and optimization of such kind of PEH systems by taking more practical factors (i.e, partial piezoelectric coverage and nonlinear conditioning interface circuits) into account.

Acknowledgement

This work is financially supported by the Energy Education Trust of New Zealand (no. 3708242) and the PhD scholarship from China Scholarship Council (no. 201608250001).

References

Abdelkefi, A., Barsallo, N., Tang, L., Yang, Y., & Hajj, M. R. (2014). Modeling, validation, and performance of low-frequency piezoelectric energy harvesters. *Journal of Intelligent Material Systems and Structures, 25*(12), 1429-1444.

duToit, N. E., Wardle, B. L., & Kim, S. G. (2005). Design considerations for MEMS-scale piezoelectric mechanical vibration energy harvesters. *Integrated Ferroelectrics, 71*(1), 121-160.

Erturk, A., & Inman, D. J. (2007). *Mechanical considerations for modeling of vibration-based energy harvesters.* Paper presented at the Proceedings of the ASME IDETC 21st Biennial Conference on Mechanical Vibration and Noise.

Erturk, A., & Inman, D. J. (2008a). A distributed parameter electromechanical model for cantilevered piezoelectric energy harvesters. *Journal of Vibration and Acoustics-Transactions of the Asme, 130*(4), 041002.

Erturk, A., & Inman, D. J. (2008b). On mechanical modeling of cantilevered piezoelectric vibration energy harvesters. *Journal of Intelligent Material Systems and Structures, 19*(11), 1311-1325.

Erturk, A., & Inman, D. J. (2009). An experimentally validated bimorph cantilever model for piezoelectric energy harvesting from base excitations. *Smart Materials and Structures, 18*(2), 025009.

Guyomar, D., Badel, A., Lefeuvre, E., & Richard, C. (2005a). Toward energy harvesting using active materials and conversion improvement by nonlinear processing. *Ieee Transactions on Ultrasonics Ferroelectrics and Frequency Control, 52*(4), 584-595.

Guyomar, D., Badel, A., Lefeuvre, E., & Richard, C. (2005b). Toward energy harvesting using active materials and conversion improvement by nonlinear processing. *Ultrasonics, Ferroelectrics, and Frequency Control, IEEE Transactions on, 52*(4), 584-595.

Hu, G., Tang, L., Banerjee, A., & Das, R. (2017). Metastructure With Piezoelectric Element for Simultaneous Vibration Suppression and Energy Harvesting. *Journal of Vibration and Acoustics, 139*(1), 011012.

Hu, G., Tang, L., Das, R., & Marzocca, P. (2018). A two-degree-of-freedom piezoelectric energy harvester with stoppers for achieving enhanced performance. *International Journal of Mechanical Sciences, 149*, 500-507.

Kim, J. E., & Kim, Y. Y. (2011). Analysis of piezoelectric energy harvesters of a moderate aspect ratio with a distributed tip mass. *Journal of Vibration and Acoustics, 133*(4), 041010.

Lan, C., Tang, L., & Harne, R. L. (2018a). Comparative methods to assess harmonic response of nonlinear piezoelectric energy harvesters interfaced with AC and DC circuits. *Journal of Sound and Vibration, 421*, 61-78.

Lan, C., Tang, L., Hu, G., & Qin, W. (2018b). *Dynamics of a bistable coupled dual-beam energy harvester and its experimental validation.* Paper presented at the Active and Passive Smart Structures and Integrated Systems XII.

Lefeuvre, E., Badel, A., Richard, C., & Guyomar, D. (2005). Piezoelectric energy harvesting device optimization by synchronous electric charge extraction. *Journal of Intelligent Material Systems and Structures, 16*(10), 865-876.

Liang, J., & Liao, W. (2012). Impedance modeling and analysis for piezoelectric energy harvesting systems. *IEEE/ASME Transactions on Mechatronics, 17*(6), 1145-1157.

Liu, H., Lee, C., Kobayashi, T., Tay, C. J., & Quan, C. (2012). Investigation of a MEMS piezoelectric energy harvester system with a frequency-widened-bandwidth mechanism introduced by mechanical stoppers. *Smart Materials and Structures, 21*(3), 035005.

Liu, W., Liu, C., Ren, B., Zhu, Q., Hu, G., & Yang, W. (2016). Bandwidth increasing mechanism by introducing a curve fixture to the cantilever generator. *Applied physics letters, 109*(4), 043905.

Liu, W., Zhao, C., Badel, A., Formosa, F., Zhu, Q., & Hu, G. (2018). Compact self-powered synchronous energy extraction circuit design with enhanced performance. *Smart Materials and Structures, 27*(4), 047001.

Priya, S. (2007). Advances in energy harvesting using low profile piezoelectric transducers. *Journal of Electroceramics, 19*(1), 167-184.

Shu, Y. C., & Lien, I. C. (2006). Analysis of power output for piezoelectric energy harvesting systems. *Smart Materials & Structures, 15*(6), 1499-1512.

Shu, Y. C., Lien, I. C., & Wu, W. J. (2007). An improved analysis of the SSHI interface in piezoelectric energy harvesting. *Smart Materials and Structures, 16*(6), 2253-2264.

Stanton, S. C., McGehee, C. C., & Mann, B. P. (2010). Nonlinear dynamics for broadband energy harvesting: Investigation of a bistable piezoelectric inertial generator. *Physica D: Nonlinear Phenomena, 239*(10), 640-653.

Tang, L., & Yang, Y. (2012). A nonlinear piezoelectric energy harvester with magnetic oscillator. *Applied physics letters, 101*(9), 094102.

Tao, K., Tang, L., Wu, J., Lye, S. W., Chang, H., & Miao, J. (2018). Investigation of multimodal electret-based MEMS energy harvester with impact-induced nonlinearity. *Journal of Microelectromechanical Systems*, *27*(2), 276-288.

Wu, Y., Qiu, J., Zhou, S., Ji, H., Chen, Y., & Li, S. (2018). A piezoelectric spring pendulum oscillator used for multi-directional and ultra-low frequency vibration energy harvesting. *Applied Energy*, *231*, 600-614.

Xu, J., & Tang, J. (2015). Multi-directional energy harvesting by piezoelectric cantilever-pendulum with internal resonance. *Applied physics letters*, *107*(21), 213902.

Yang, Y., & Tang, L. (2009). Equivalent Circuit Modeling of Piezoelectric Energy Harvesters. *Journal of Intelligent Material Systems and Structures*, *20*(18), 2223-2235.

Yang, Y., Zhao, L., & Tang, L. (2013). Comparative study of tip cross-sections for efficient galloping energy harvesting. *Applied physics letters*, *102*(6), 064105.

Zhao, L., Tang, L., & Yang, Y. (2013). Comparison of modeling methods and parametric study for a piezoelectric wind energy harvester. *Smart Materials and Structures*, *22*(12), 125003.

Zhao, L., Tang, L., & Yang, Y. (2016). Synchronized charge extraction in galloping piezoelectric energy harvesting. *Journal of Intelligent Material Systems and Structures*, *27*(4), 453-468.

Zhao, L., & Yang, Y. (2015). Enhanced aeroelastic energy harvesting with a beam stiffener. *Smart Materials and Structures*, *24*(3), 032001.

Zhou, S., Cao, J., Erturk, A., & Lin, J. (2013). Enhanced broadband piezoelectric energy harvesting using rotatable magnets. *Applied physics letters*, *102*(17), 173901.

Zhou, S., & Wang, J. (2018). Dual serial vortex-induced energy harvesting system for enhanced energy harvesting. *AIP Advances*, *8*(7), 075221.